



## Article

# Long-Term and Emergency Monitoring of Zhongbao Landslide Using Space-Borne and Ground-Based InSAR

Ting Xiao <sup>1,2,3</sup>, Wei Huang <sup>4</sup>, Yunkai Deng <sup>2,3,\*</sup> , Weiming Tian <sup>3</sup> and Yonglian Sha <sup>1</sup>

<sup>1</sup> Beijing Institute of Technology Chongqing Innovation Center, Chongqing 401135, China; tingxiao@bit.edu.cn (T.X.); syl973281310@163.com (Y.S.)

<sup>2</sup> Chongqing Key Laboratory of Geological Environment Monitoring and Disaster Early-Warning in Three Gorges Reservoir Area, Chongqing Three Gorges University, Chongqing 404000, China

<sup>3</sup> Radar Research Lab, School of Information and Electronics, Beijing Institute of Technology, Beijing 100081, China; tianweiming@bit.edu.cn

<sup>4</sup> Chongqing Institute of Geology and Mineral Resources, Chongqing 400042, China; huangwei@cug.edu.cn

\* Correspondence: yunkai\_bit@bit.edu.cn; Tel.: +86-130-4103-5875

**Abstract:** This work presents the ideal combination of space-borne and ground-based (GB) Interferometric Synthetic Aperture Radar (InSAR) applications. In the absence of early investigation reporting and specialized monitoring, the Zhongbao landslide unexpectedly occurred on 25 July 2020, forming a barrier lake that caused an emergency. As an emergency measure, the GB-InSAR system was installed 1.8 km opposite the landslide to assess real-time cumulative deformation with a monitoring frequency of 3 min. A zone of strong deformation was detected, with 178 mm deformation accumulated within 15 h, and then a successful emergency warning was issued to evacuate on-site personnel. Post-event InSAR analysis of 19 images acquired by the ESA Sentinel-1 from December 2019 to August 2020 revealed that the landslide started in March 2020. However, the deformation time series obtained from satellite InSAR did not show any signs that the landslide had occurred. The results suggest that satellite InSAR is effective for mapping unstable areas but is not qualified for rapid landslide monitoring and timely warning. The GB-InSAR system performs well in monitoring and providing early warning, even with dense vegetation on the landslide. The results show the shortcomings of satellite InSAR and GB-InSAR and a clearer understanding of the necessity of combining multiple monitoring methods.

**Keywords:** landslide; emergency; Interferometric Synthetic Aperture Radar; space-borne; ground-based



**Citation:** Xiao, T.; Huang, W.; Deng, Y.; Tian, W.; Sha, Y. Long-Term and Emergency Monitoring of Zhongbao Landslide Using Space-Borne and Ground-Based InSAR. *Remote Sens.* **2021**, *13*, 1578. <https://doi.org/10.3390/rs13081578>

Academic Editors: Federica Bardi, Pierluigi Confuorto, Giulia Dotta, Diego Di Martire and Qingkai Meng

Received: 22 March 2021

Accepted: 17 April 2021

Published: 19 April 2021

**Publisher's Note:** MDPI stays neutral with regard to jurisdictional claims in published maps and institutional affiliations.



**Copyright:** © 2021 by the authors. Licensee MDPI, Basel, Switzerland. This article is an open access article distributed under the terms and conditions of the Creative Commons Attribution (CC BY) license (<https://creativecommons.org/licenses/by/4.0/>).

## 1. Introduction

The Three Gorge Reservoir (TGR) area in China has complex geological and hydrological environments, resulting in a large number of landslides, such as the famous Xintan landslide [1,2], Qianjiangping landslide [3,4], and Jiweishan landslide [5,6]. In the TGR area, more than 5000 potential disasters are being monitored by specialized equipment and a community-based disaster risk reduction system [7–10]. Nevertheless, heavy rains and fluctuation in the reservoir level still cause several “unknown” landslides to unexpectedly occur every year [11–13]. Landslides with a long history of deformation can be controlled by engineering means or other disaster mitigation methods before major damage occurs [14,15]. However, for some landslides, the time between the beginning of deformation and destruction is only a few months [16,17]. The surface damage characteristics of a rapid landslide located in a sparsely populated area are not easily identified, leading to sudden damage and casualties [18,19].

Deep inclinometers, GNSS/GPS stations, automatic crack meters, and inclinometers are among the conventional equipment used to monitor landslide movements [20–22]. These devices are installed on past landslides or landslides with signs of movement, so new landslides that occur suddenly often lack these data. After the major failure of a

slope, its physical and mechanical parameters are irreversibly weakened. Changes in the stress distribution make the slope unstable as well, resulting in the potential risk of secondary landslides [23–25]. In landslide emergency rescue, it is necessary to monitor slope movements in real time and with high frequency to ensure the safety of affected communities or workers cleaning the landslide dam.

Over the past decade, monitoring and remote-sensing techniques for landslide analysis have developed rapidly, among which Interferometric Synthetic Aperture Radar (InSAR) techniques are increasingly being applied [26–29]. The InSAR method was originally developed from data obtained from a space-borne platform, and it was later applied on a ground platform (GB-InSAR). A GB-InSAR system can be installed within a distance from tens of meters to several kilometers, which provides flexibility in choosing observation angles. This system works in the microwave band and is not affected by weather conditions during imaging, so it has the advantage of all-weather and all-time operation [30]. GB-InSAR can acquire an image every few minutes to continuously observe the target area in real time. Benefiting from the characteristics of non-contact measurement, high (minute-level) monitoring frequency, and sub-millimeter accuracy, the GB-InSAR system has become increasingly popular for monitoring local landslides [31] and unstable slopes [32] in the past few years, especially in disaster emergency rescue work [33,34]. Space-borne InSAR has proven effective for identifying landslides in large-scale mountain areas, as well as for early monitoring [35,36]. Some landslides occur rapidly with a short acceleration period, and the long revisiting period means that satellite InSAR is not able to monitor such landslides in real time. Space-borne InSAR and GB-InSAR are applied at different spatial scales, and their combination can provide more comprehensive and specific data.

This paper aims to describe the main kinematic characteristics of the Zhongbao landslide through combined observations of Sentinel-1 satellite InSAR and GB-InSAR. The GB-InSAR system proved its important role in real-time emergency monitoring through a successful early warning in this case. The satellite InSAR observations revealed when the landslide began to develop, but it failed to verify the acceleration and damage of the landslide due to the decoherence of two images caused by the large deformation. The analysis particularly shows the shortcomings of satellite InSAR and GB-InSAR and a clearer understanding of the necessity of combining multiple monitoring methods.

## 2. Description of Zhongbao Landslides

Numerous cracks and macroscopic surface deformation began to appear on the trailing edge of the Zhongbao landslide on 22 July 2020. Due to strong sustained rainfall, the landslide suddenly occurred on July 25, which disturbed village roads and completely blocked the Yancang River, forming a barrier lake with a water level difference of 13 m and a reservoir capacity of  $55 \times 10^4 \text{ m}^3$ . A total of 520 people from 162 households were urgently evacuated. If the barrier dam were to break, the area, as well as QuanTang power station, would be in danger of flooding. The Zhongbao landslide occurred suddenly and is geologically brand new, without early investigation reports or monitoring data. After the occurrence of the landslide on the 25th, the municipal government immediately organized the barrier dam clearing, population transfer, and emergency monitoring.

### 2.1. Location and Topographic Features

The Zhongbao landslide ( $29^\circ 28' 53'' \text{ N}$  and  $107^\circ 55' 43'' \text{ E}$ ) is located on the north side of the Yancang River in the Zhongtai Group of Liuqing Village, Tudi Township, Wulong County, Chongqing City (China), about 136 km from the city center (Figure 1). The study area extends to the subtropical humid monsoon zone and features a mild climate with abundant sunshine and mean annual precipitation of 1000–1200 mm, mainly concentrated from April to July. The landslide has a maximum length and width of 900 m and 340 m, respectively, covering a total area of approximately  $26 \times 10^4 \text{ m}^2$  with an estimated volume of  $130 \times 10^4 \text{ m}^3$ . The landslide is located in the Qinggang syncline, without any regional or small faults. The slope angle of the landslide ranges from  $20^\circ$ – $40^\circ$ , and a locally steep

section can exceed  $50^\circ$ . The landslide mass was mainly composed of cataclastic rock mass and Quaternary deposits, including silty clay and rubble soil, overlaying the bedrock consisting of Silurian Lower Hanjiadian Formation ( $S_1h$ ) shale.

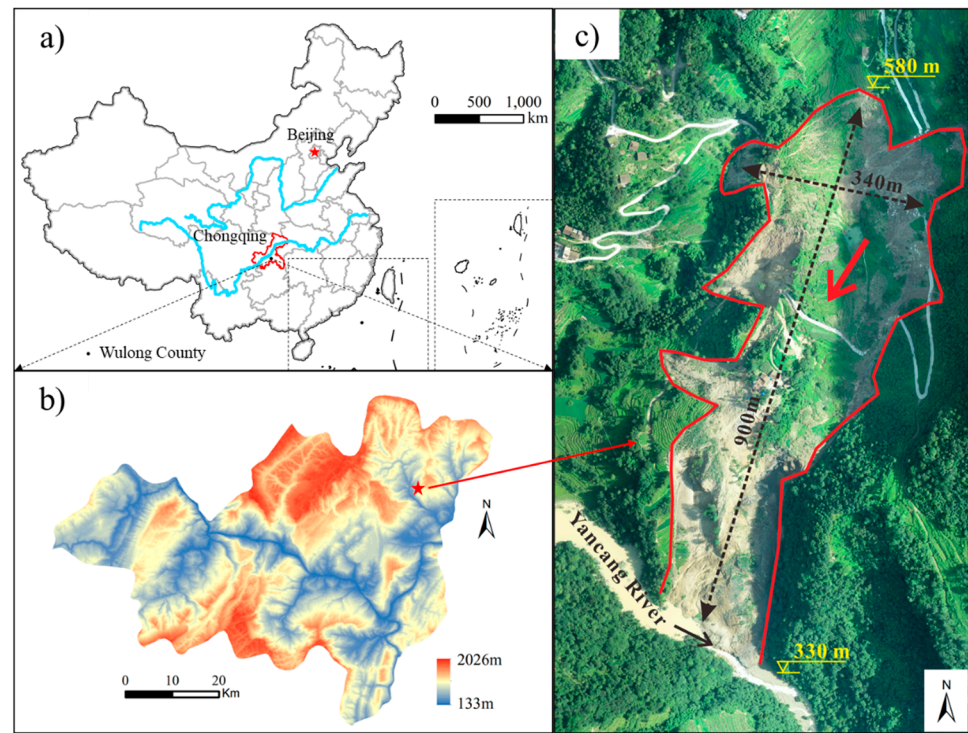


**Figure 1.** Location of Zhongbao landslide. (a) Location of Wulong County. (b) Location of Zhongbao landslide. (c) Topographic feature of Zhongbao landslide.

## 2.2. Field Survey and Deformation Characteristics

There was one main sliding body and three secondary sliding bodies in the landslide (Figure 2a). The main sliding body moved toward the Yancang River in the south, and the three secondary slides moved westward and were driven by the terrain. The trailing edges of these slides can be easily identified by scarps (Figure 2b) and scratches (Figure 2c). The forest on the trailing edge of the main landslide was displaced by a distance of 100 m, with a height difference of 52 m. Measured from a three-dimensional topographic map obtained by a drone, the slope angles of ZB#1 and ZB#2 are over  $45^\circ$ , and that of ZB#3 is around  $30^\circ$ . Furthermore, with a drop of more than 60 m, their impact force cannot be overlooked. In the middle of the landslide, the soil was compressed to the point of bulging, visible to the naked eye in several places (Figure 2d). According to villagers' accounts, the first macroscopic surface deformation appeared on the trailing edge, which is a feature of the thrust load that caused the landslide. Several houses located in the middle of the landslide were destroyed (Figure 2e). Some highways were torn to pieces, and others were severely cracked (Figure 2f).

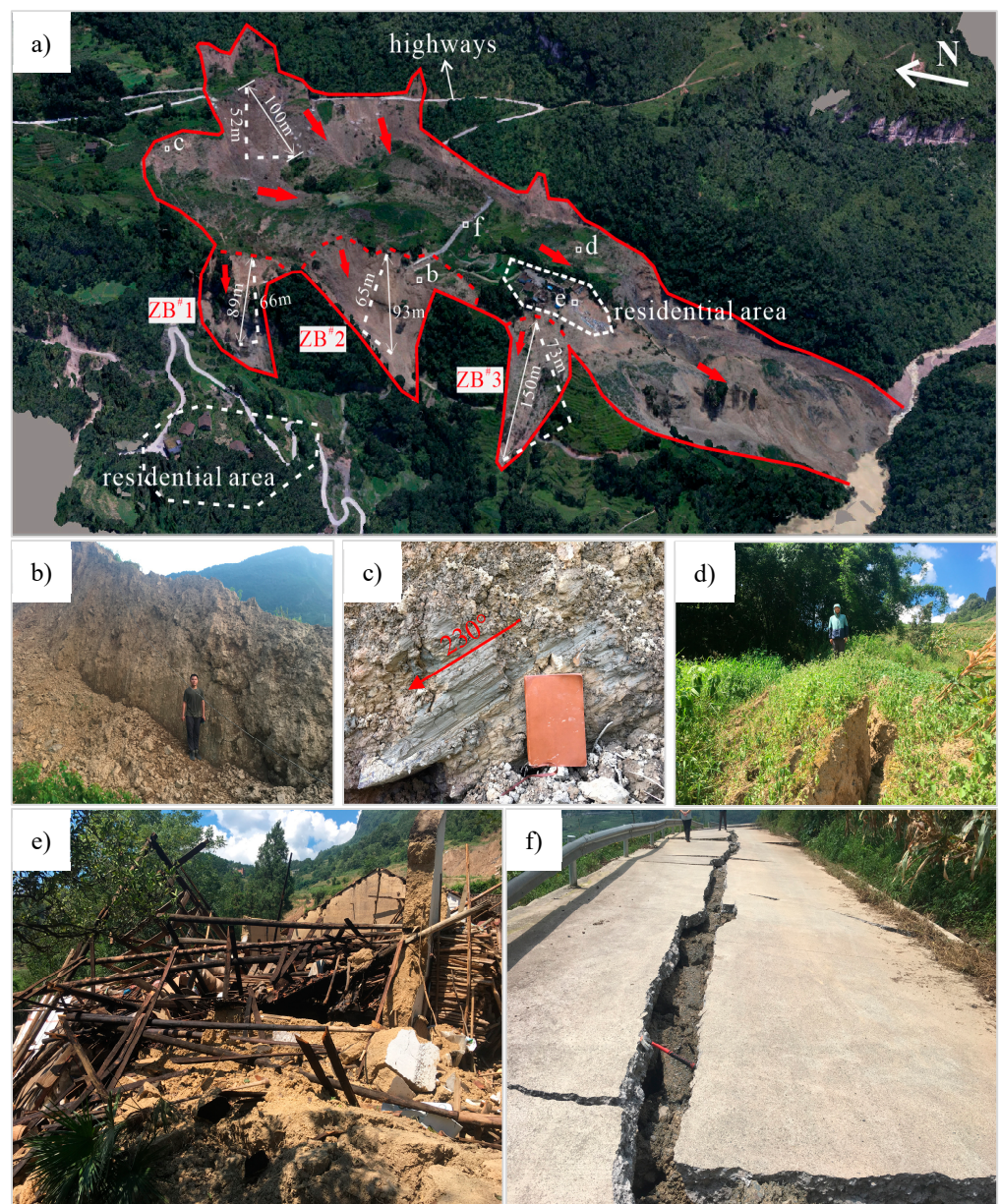


**Figure 2.** Hazard-bearing body and macroscopic deformations of the Zhongbao landslide. (a) Plane map of the Zhongbao landslide. (b) Silty clay and rubble at the scarp. (c) Scratches at  $230^\circ$  on the trailing edge of the landslide. (d) The slope in the middle of the landslide was compressed to the point of bulging. (e) Destroyed houses. (f) Cracks on a road.

### 3. Emergency Monitoring

After the landslide occurred, a GB-InSAR (ground-based interferometric synthetic aperture radar) system was used for emergency monitoring to obtain the stability dynamics of the landslide in real time (Figure 3). The instrument was developed by Beijing Institute of Technology and was provided by Suzhou Institute of Technology Reco Sensing Technology Co., Ltd. As a developed type of high-accuracy deformation measurement system, GB-InSAR has been widely utilized to monitor surface deformations of natural or artificial slopes.



**Figure 3.** GB-InSAR system employed in the emergency monitoring.

The system was installed 1.8 km opposite the landslide and equipped with a network cable, laptop, and a power supply. The upper computer software was used to calculate the deformation information, which was displayed on a laptop screen in real time. The main technical features of the GB-InSAR system are listed in Table 1.

**Table 1.** Parameters of the employed radar system.

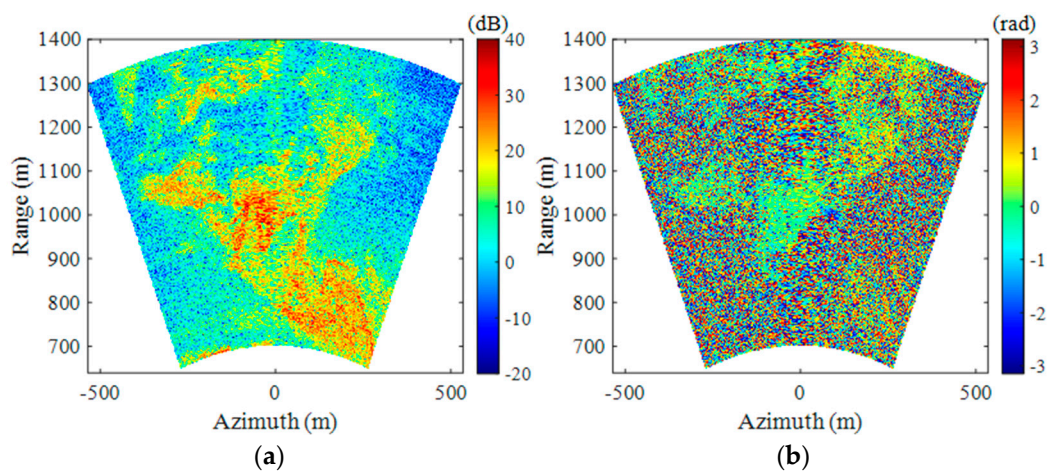
Parameters	Value
Rail length	1.8 m
Band	Ku
Central frequency	16.2 GHz
Bandwidth	600 MHz
Image acquisition time	3 min
Resolution	0.25 m × 5 mrad@1km
Power	200 W

From 16:16 on 27 July 2020 to 19:46 on 30 July 2020 (China Standard Time), emergency monitoring was implemented with the GB-InSAR system. Due to a field power failure, the whole monitoring period was divided into three parts, as shown in Table 2. A total of 628 images were acquired over a monitoring period of 3 days.

**Table 2.** Monitoring periods selected for analysis.

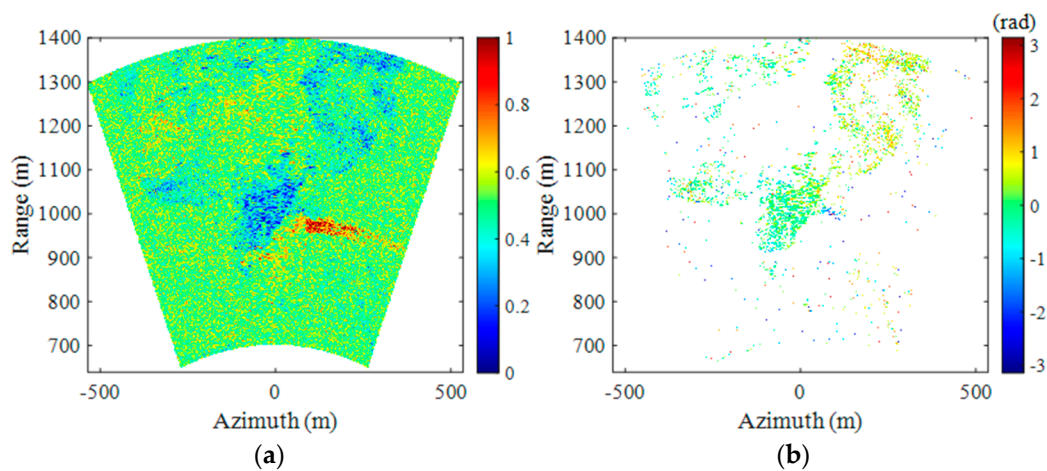
	Monitoring Period	Total Time	Image Number
1	27 July, 16:00 to 28 July, 7:00	15 h	296
2	28 July, 11:00 to 28 July, 18:00	7 h	126
3	30 July, 07:12 to 30 July, 19:46	12 h	206

Figure 4a shows a power image of the monitoring area at the rectangular coordinate, which was dB processed with respect to the average noise level and can be regarded as a signal-to-noise ratio (SNR) map. From the SNR map, we can preliminarily judge where the bare slopes are located in the radar image. With two radar images acquired at different times and from the same position, their differential phases can be explored to measure one-dimensional deformations based on the differential interferometry technique. Figure 4b shows a phase interferogram formed by the first and second images, whose temporal baseline is just several minutes. The phases of pixels located on the bare slope are around 0 rad, and those located on the vegetation regions vary randomly.



**Figure 4.** (a) Power image of the monitoring area; (b) phase interferogram.

Not all pixels in a GB-InSAR interferogram are suitable for phase analysis. To guarantee measurement accuracy, only pixels with high phase quality are processed. The ADI (amplitude dispersion index) method is commonly utilized to select appropriate pixels, also known as permanent scatterers (PSs). A pixel's ADI is defined as the ratio between the standard deviation and mean value of its time-series amplitudes. A smaller ADI means a higher phase stability. Figure 5a shows the ADI map calculated with the first 30 radar images. By setting an ADI threshold of 0.35 and an SNR threshold of 10 dB, sufficient PSs were selected. Figure 5b shows the PS phase map. Notably, almost all the PSs are located on the bare slopes.



**Figure 5.** (a) The amplitude dispersion index map; (b) permanent scatterer phase map.

Based on the differential interferometry technique, GB-InSAR images were processed together. Figure 6 shows the cumulative deformation map. Three regions with large deformations can be observed, where negative deformation indicates that the direction is toward the radar. Figure 7 shows the deformation curves of three typical points during three monitoring periods.

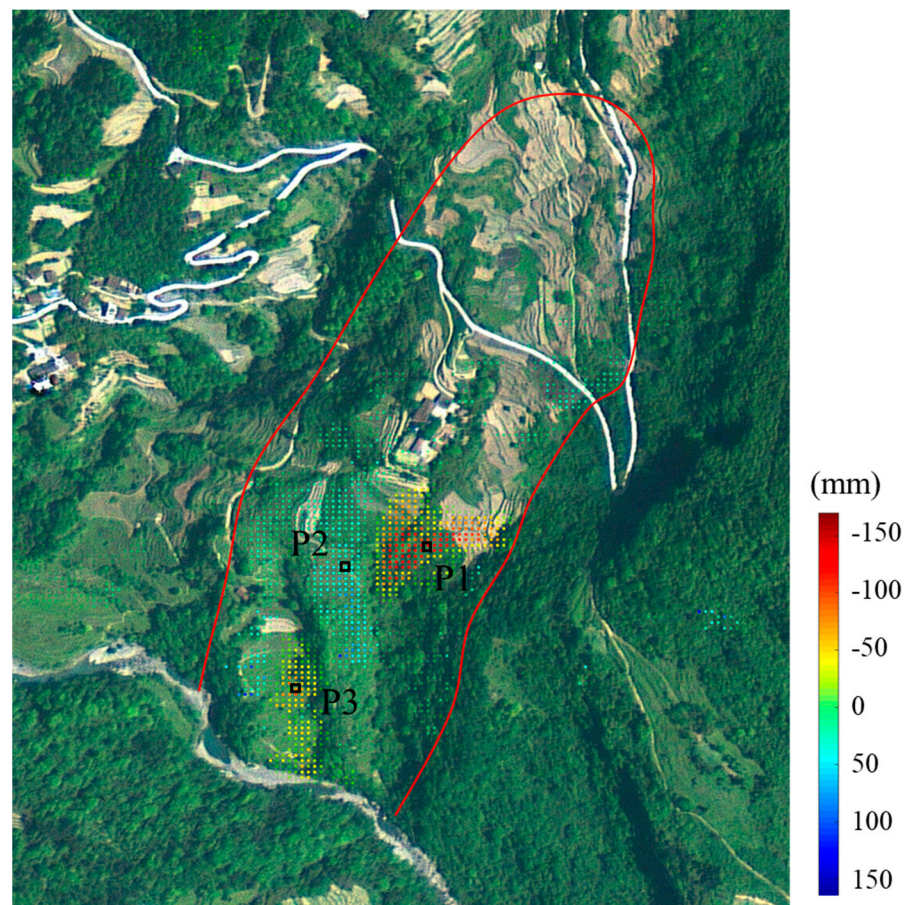


**Figure 6.** Cumulative displacement map of GB-InSAR campaigns.

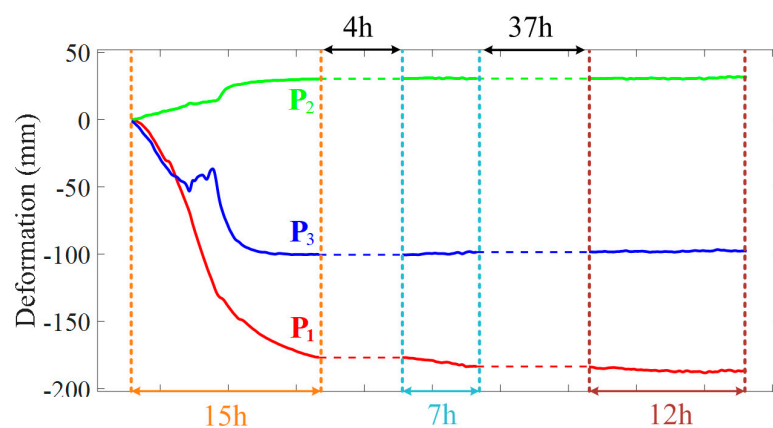


**Figure 7.** Deformation time series of typical points.

The deformation recorded by GB-InSAR is the change in the distance from the slope surface to the line of sight (LOS) of the radar, rather than the real absolute displacement of slope surface, which is provided by GNSS/GPS. Although GB-InSAR does not record the true absolute displacement, it still effectively reflects the deformation trend of the landslide.

P1 accumulated 178 mm of deformation in 15 h in period 1 and even reached 30 mm/h around 21:30 on 27 July. In period 2, the cumulative displacement of P1 within 7 h was only 6.85 mm, which means that the movement of P1 had greatly slowed down. The cumulative displacement within 12 h in period 3 did not exceed 3 mm. The cumulative deformation (30.2 mm) of P2 during period 1 was much lower than that of P1, and almost

no deformation occurred in the second half. The typical point P2 remained stable during periods 2 and 3, with cumulative displacements of 0.3 mm and 1.3 mm, respectively. P3 accumulated 100.2 mm, 1.7 mm, and 0.7 mm in periods 1, 2, and 3, respectively. It can be seen from the deformation time series in Figure 7 that P1 had the strongest movements, which gradually slowed in period 2 and stabilized in period 3. P2 and P3 tended to stabilize in the second half of period 1, and there was almost no deformation in Periods 2 and 3. In general, it can be inferred from the three typical points that the landslide was generally stable on 30 July.

It is worth mentioning that when P1 was monitored during period 1, the excessive displacement attracted a lot of attention from on-site monitoring staff, and then investigators within the affected area of the landslide were asked to leave. The GB-InSAR system provided a successful emergency warning, which can be confirmed in Figure 8. The topography of the deformation zone where point P1 is located changed visibly between noon on the 27th and the 28th, which can be seen from the optical image.

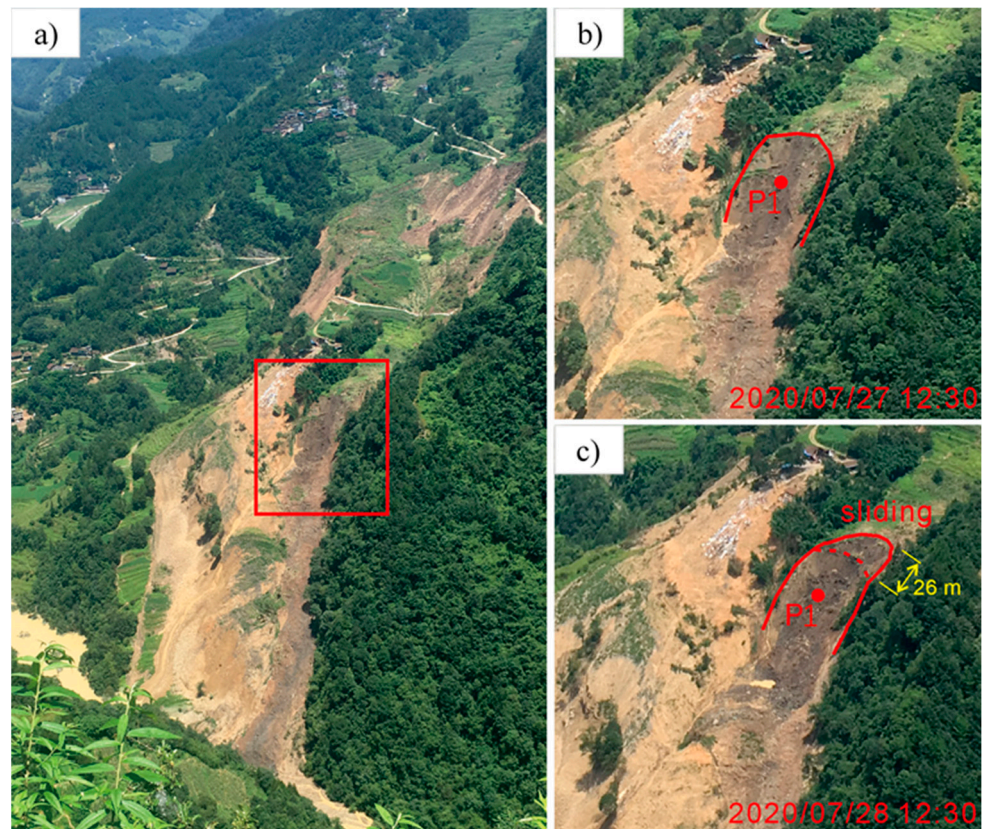


**Figure 8.** Optical image of the Zhongbao landslide. (a) The location of the deformation zone. (b) Deformation zone at 12:30 on July 27. (c) Deformation zone at 12:30 on July 28.

According to villagers' accounts, the first macroscopic surface deformation appeared on the trailing edge, and huge bulging cracks on the middle landslide were found in the field investigation (Figure 2d). Therefore, it can be safely inferred that the energy that started the Zhongbao landslide was located at the trailing edge, which is the feature of the thrust load that caused the landslide. During the emergency monitoring period, although there was local movement at the center, it did not pull the rear part, so the landslide was presumed to be stable overall. Despite this inference, seven GNSS stations and one rain gauge were installed in the next few days to control the landslide risk. As shown in Figure 9, the rain gauge and G01 were installed in the residential area outside the landslide, and the remaining G02–G07 points were distributed on the landslide body. There was almost no displacement change at G01, which suggested that the landslide would not affect

the residential area outside the boundary. The deformation time series of G02–G07 can be seen in Figure 10. The cumulative displacement of the landslide over a month was less than 3 mm, except for G07. The rain gauge detected 10 mm and 5 mm rainfall on August 20 and August 24, but the displacement time series did not register it. Slope failure is the process of internal stress release, and the landslide is currently stabilizing after the past failure.

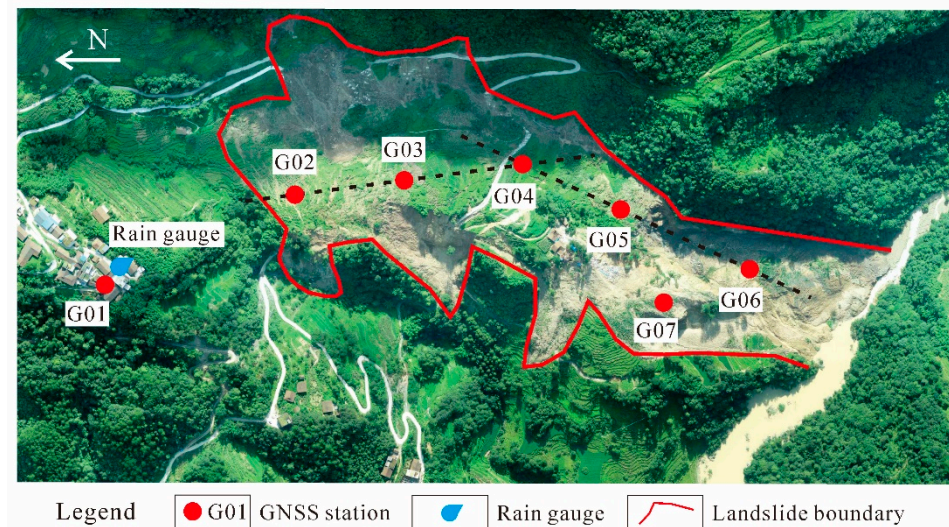


Figure 9. GNSS monitoring system on the Zhongbao landslide.

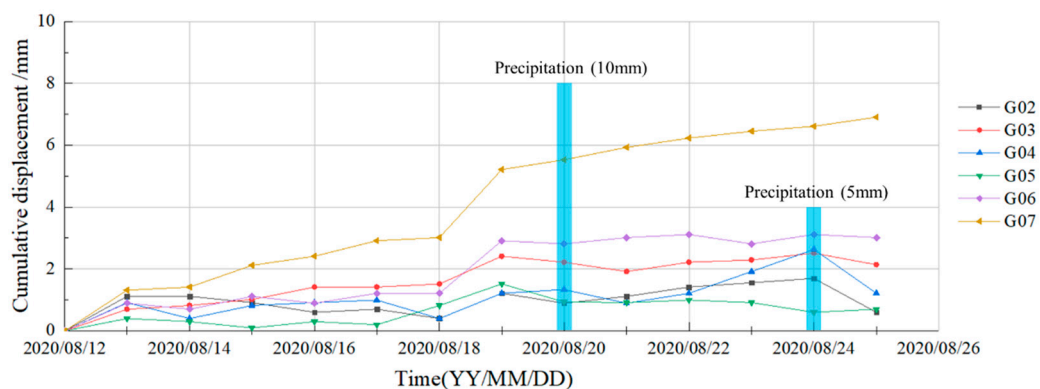


Figure 10. Deformation time series of GNSS stations on the Zhongbao landslide.

#### 4. Deformation History

The Zhongbao landslide was totally unexpected: it was not in the landslide inventory, so there were no early investigation reports or monitoring data. The GB-InSAR system was installed as an emergency measure after the landslide caused significant damage, which is useless for a historical deformation analysis. Satellite datasets are the sole available channel for obtaining the deformation history of the Zhongbao landslide. After the event, a multi-interferogram analysis of C-band SAR images acquired by Sentinel-1 satellites was performed (Table 3). More precisely, the analysis was carried out on Sentinel-1 images acquired in the Interferometric Wide (IW) swath mode, the main acquisition mode over land, which acquires data with a  $250 \text{ km} \times 170 \text{ km}$  scope at  $5 \text{ m} \times 20 \text{ m}$  spatial resolution. The available archive of Sentinel-1, including 19 images collected from December 2019 to August 2020, was acquired and processed. Images were captured in the ascending orbit with an azimuth of  $-12.64^\circ$  and an incidence angle of  $33.87^\circ$ . These images were taken at intervals of 12 days for 228 days in total, which includes 2 images after the event. The European Space Agency's precision orbit data were used to correct the orbit of Sentinel-1A

images. Additionally, the interference of the terrain phase was reduced by SRTM digital elevation data with an accuracy of 30 m.

**Table 3.** Parameters of Sentinel-1A images.

Parameters	Sentinel-1A Images
Orbit	ascending
Band	C
Wavelength	5.6 cm
Resolution	5 m × 20 m
Revisiting interval	12 d
Course angle	−12.64°
Incidence angle	33.87°

The Sentinel-1A data were processed by applying the SBAS (Small Baseline Subset) method to obtain a more continuous spatial sequence diagram of deformation, thereby removing the decoherence problem caused by the excessively long spatial baseline in the DInSAR method. In this case, the SBAS spatio-temporal baseline thresholds were set to 60 days and 190 m, respectively, forming a baseline network composed of 41 interference pairs (Figure 11). The landslide surface deformation and time series were acquired using differential image processing and the singular value decomposition method. The spatial distribution of persistent scatterer (PS) points and their mean velocities can be seen in Figure 12. The number of PS points on the landslide is sparser than that in the area beyond the right boundary of the landslide, which is caused by the dense vegetation and almost north-south slope aspect. Nevertheless, most of the PS points with large deformations are located in the landslide area. Five typical points in different parts of the landslide were selected for deformation time-series analysis (Figure 13).

Before the landslide event, there were no rain gauges to obtain accurate rainfall data at the local landslide area. Figure 13 shows the average rainfall of Wulong District (monitored by the local meteorological station in Wulong District) and roughly represents the 6-month precipitation trend in the landslide area. Figure 13 reveals that the intensified deformation of typical points started with the persistent rainfall in March. Thereafter, the cumulative displacement increased linearly under the influence of continuous heavy rain from May to July. Since two images of the series were captured after the landslide (July 25), the curve should show significant acceleration and deceleration around the event, according to the literature and practical monitoring. However, the deformation time series of typical points registered by Sentinel-1 does not show such characteristics. It is difficult to confirm the status of landslide stability and make an early warning decision on the basis of cumulative displacement without any acceleration indicators.

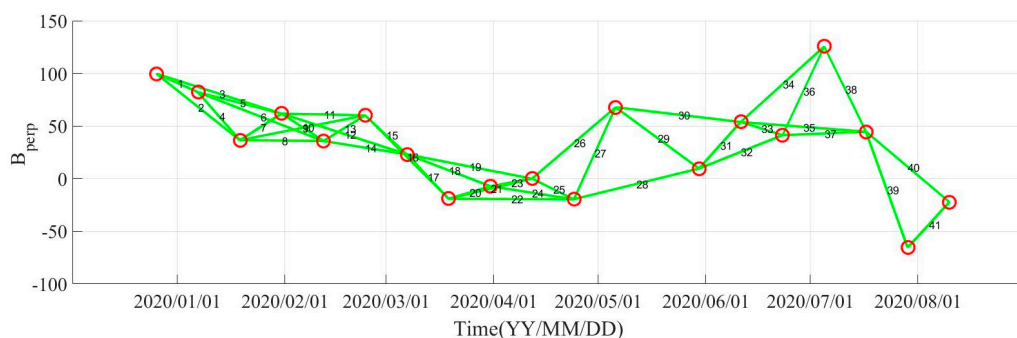


**Figure 11.** The space-time baseline map of Sentinel-1A images.

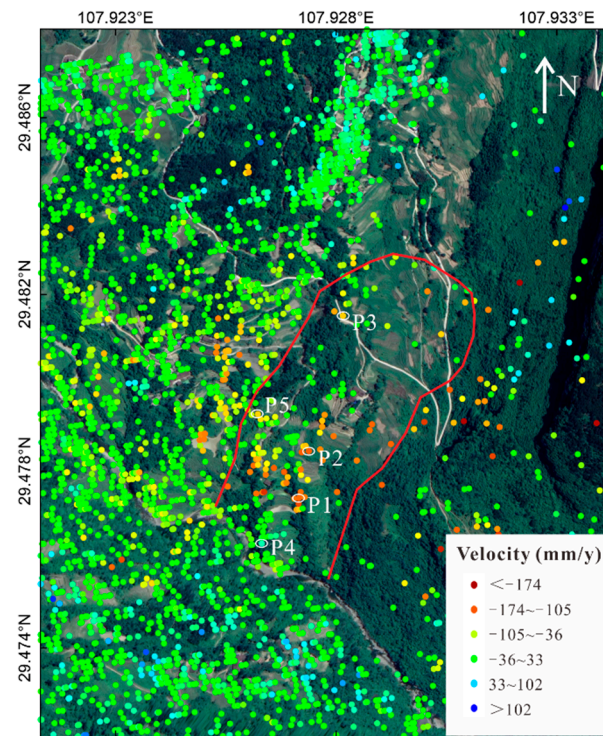


Figure 12. Mean velocities registered by Sentinel-1 satellites.

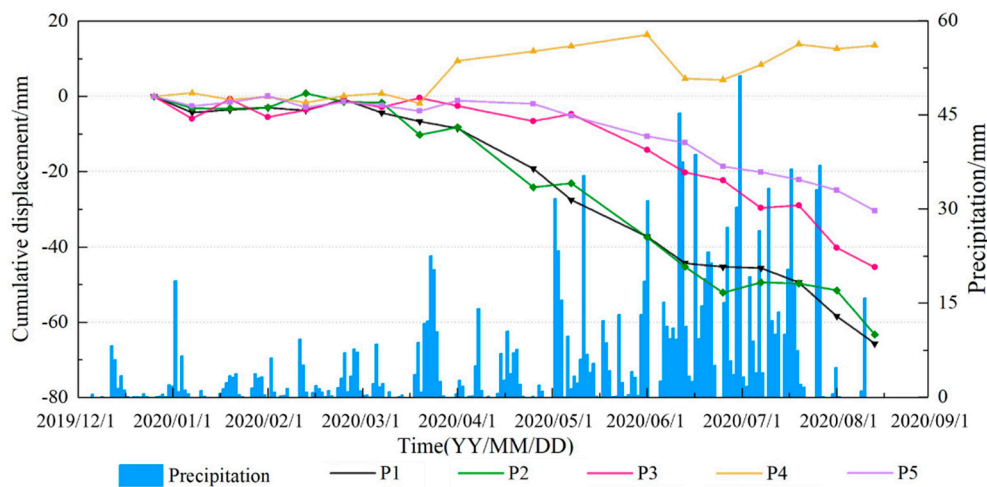


Figure 13. Mean velocities registered by the Sentinel-1A satellite.

### 5. Discussion

The southwest mountainous area of China has a complex geological, geomorphic environment and has suffered various geological disasters. Due to the vast territory, it is currently difficult to detect all geological disasters in every corner of the region. Coupled with the interference of external factors, landslides that we "do not know" about often occur unexpectedly, which seriously threatens the safety of life and property. After the disaster occurs, there is still the potential danger of secondary disasters before it stops completely. If the landslide body enters the river and causes a landslide dam, the dam needs to be dismantled as soon as possible; otherwise, it may threaten lives and the economy of downstream areas. In the absence of previous geological surveys and an understanding of the properties of landslide rock and soil parameters, surface deformation is the most accessible information to assist in judging the stability of the landslide.

The installation of conventional GNSS/GPS equipment requires several days, and the installer working on the landslide will be at risk from a secondary landslide, which prevents these systems from being used for emergency monitoring. For landslide emergency monitoring, the equipment should meet the requirements of fast installation, high accuracy, and high frequency, which are the exact advantages of GB-InSAR. In this case, the successful secondary warning of the Zhongbao landslide based on the deformation data registered by GB-InSAR proves its performance. It is worth noting that the deformation recorded by GB-InSAR is the change in the distance from the slope surface to the line of sight (LOS) of the radar, rather than the real absolute displacement of the slope surface, which is provided by GNSS/GPS. The real displacement of the slope surface is usually much larger than the elevation changes along the LOS of the radar system. For instance, for the landslide discussed in this paper, the maximum displacement recorded by GB-InSAR was 170 mm, but the actual trailing edge of the slide slipped by about 26 m (Figures 7 and 8). Therefore, the monitoring information recorded by GB-InSAR can reflect the deformation area of the landslide surface and its deformation trend, but it only indicates the elevation changes along the LOS of the radar, which is quite different from the absolute displacement provided by GNSS/GPS.

The employed GB-InSAR cannot penetrate vegetation well because the Ku-band wavelength is too short. In this case, the vegetation of the Zhongbao landslide is very dense. If the GB-InSAR system had been used before the landslide occurred, the monitoring performance would have been poor due to insufficient PS points. However, as a result of the destruction caused by the landslide, vegetation was buried or slipped and accumulated, and more exposed soil and bedrock appeared, so GB-InSAR was able to detect the deformation of more areas on the landslide. This is a very interesting perspective: dense vegetation on landslides can prevent the application of GB-InSAR, but the problem will disappear when the landslide occurs. Typical application scenarios of GB-InSAR are bare rock slopes, mine pits, and other slopes with little vegetation. The Zhongbao landslide, as a soil slope with dense vegetation, is a rare GB-InSAR application scenario in the literature. Although GB-InSAR was only used for emergency monitoring in this case, it still played a major role in issuing a successful emergency warning for partial sliding.

The GB-InSAR system has outstanding advantages in monitoring, but the equipment is very expensive and the monitoring scope of a single device is limited, so its large-scale use is not practical. Currently, GB-InSAR is commonly employed in the emergency or regular monitoring of several important landslides. Meanwhile, we are carrying out an intermittent monitoring experiment based on the GB-InSAR system. The target landslide is monitored for several hours a week. The radar is fixed through a cement observation pier to ensure that the radar position is the same every time. If the GB-InSAR system is fixed in one place for continuous operation, only one landslide can be monitored. By means of the intermittent monitoring method, several landslides can be monitored by one device at the same time, thereby reducing the cost of using the GB-InSAR system.

Space-borne InSAR can detect landslide deformation on a large scale, and research costs can be reduced by using free Sentinel data, which complements the GB-InSAR system. Usually, we can obtain free Sentinel data with a revisiting time of 12 or 6 days (when both sensors are active over the same area), which is an adequate interval for the early identification of landslides. Although the Zhongbao landslide has a north–south slope with dense vegetation, Sentinel-1A also allowed for early identification. Based on the mean velocities registered by the Sentinel-1A satellite, it is easy to infer that the deformation of the landslide started with the persistent rainfall in March and continued to progress until July. The landslide caused serious damage on July 25, but the monitoring curve by Sentinel-1A did not show any signs that the landslide had occurred. In fact, the deformation during the revisiting period exceeds half the wavelength, resulting in decoherence of the two images and inaccurate predictions. Therefore, after the space-borne InSAR achieves early recognition, it must be supplemented with other high-frequency monitoring methods (such as GB-InSAR) to effectively control and prevent disasters. It is difficult to proceed from

identification to early warning by InSAR satellites alone. Every system must be designed purposefully for specific needs rather than all needs. Space-borne InSAR and GB-InSAR are perfectly complementary systems in geological-hazard monitoring: Space-borne InSAR first finds hidden landslides from large-scale areas, and then GB-InSAR performs high-precision and high-frequency real-time deformation monitoring to analyze the development trend of the landslide for a timely warning and forecast before the disaster happens.

## 6. Conclusions

The Zhongbao landslide occurred on 25 July 2020 in Wulong County, Chongqing (China). The landslide happened suddenly, resulting in the formation of a barrier lake that caused an emergency. In emergency rescue work, traditional monitoring equipment cannot be installed on the landslide or be implemented normally in a very short time. The GB-InSAR system was installed 1.8 km opposite the landslide to obtain real-time deformation data from the landslide surface. It provided a successful emergency warning for partial sliding, thereby protecting the safety of on-site personnel. After the event, multi-interferometry of the C-band SAR images acquired by Sentinel-1 satellites was performed to analyze the deformation history of the Zhongbao landslide. The space-borne InSAR results indicate that the landslide had been active since March 2020, but it failed to show any signs of acceleration following the landslide in July.

It is worth remembering that no monitoring system is valid for all cases. Every system must be designed purposefully for specific needs rather than all needs. Space-borne InSAR and GB-InSAR are perfectly complementary systems in geological hazard monitoring. Space-borne InSAR can be used for the early identification of disasters in large-scale areas, but due to its long revisiting period it is not very effective for identifying sudden destruction. On the contrary, GB-InSAR plays a major role in emergency monitoring and is characterized by easy installation, high precision, and high frequency. This paper presents an ideal combination of space-borne and ground-based InSAR applications. The results show their respective shortcomings and provide a clearer understanding of the necessity of combining multiple monitoring methods.

**Author Contributions:** T.X. organized and analyzed the data and wrote the paper; W.H. provided and analyzed the data; Y.D. analyzed the data and wrote the paper; W.T. was responsible for the project; Y.S. analyzed the data. All authors have read and agreed to the published version of the manuscript.

**Funding:** This work was supported by the National Natural Science Foundation of China (grant numbers: 61971037, 61960206009, 31727901), Natural Science Foundation of Chongqing, China (grant number cstc2020jcyj-jqX0008), and Chongqing Key Laboratory of Geological Environment Monitoring and Disaster Early-warning in Three Gorges Reservoir Area (No. MP2020B0301).

**Data Availability Statement:** Restrictions apply to the availability of these data. Data were obtained from Chongqing Institute of Geology and Mineral Resources and are available from the authors with the permission of Chongqing Institute of Geology and Mineral Resources.

**Acknowledgments:** We wish to thank the Chongqing Institute of Geology and Mineral Resources for their landslide investigation.

**Conflicts of Interest:** The authors declare no conflict of interest.

## References

1. Huang, Z.; Law, K.T.; Liu, H.; Jiang, T. The chaotic characteristics of landslide evolution: A case study of Xintan landslide. *Environ. Geol.* **2009**, *56*, 1585–1591. [[CrossRef](#)]
2. Keqiang, H.; Shangqing, W.; Wen, D.; Sijing, W. Dynamic features and effects of rainfall on landslides in the Three Gorges Reservoir region, China: Using the Xintan landslide and the large Huangya landslide as the examples. *Environ. Earth Sci.* **2010**, *59*, 1267–1274. [[CrossRef](#)]
3. Wang, F.W.; Zhang, Y.M.; Huo, Z.T.; Matsumoto, T.; Huang, B.L. The July 14, 2003 Qianjiangping landslide, three gorges reservoir, China. *Landslides* **2004**, *1*, 157–162. [[CrossRef](#)]

4. Keqiang, H.; Sijing, W. Double-parameter threshold and its formation mechanism of the colluvial landslide: Xintan landslide, China. *Environ. Geol.* **2006**, *49*, 696–707. [[CrossRef](#)]
5. Kulatilake, P.H.; Ge, Y. Investigation of stability of the critical rock blocks that initiated the Jiweishan landslide in China. *Geotech. Geol. Eng.* **2014**, *32*, 1291–1315. [[CrossRef](#)]
6. Yin, Y.; Sun, P.; Zhang, M.; Li, B. Mechanism on apparent dip sliding of oblique inclined bedding rockslide at Jiweishan, Chongqing, China. *Landslides* **2011**, *8*, 49–65. [[CrossRef](#)]
7. Liu, Y.; Yin, K.; Chen, L.; Wang, W.; Liu, Y. A community-based disaster risk reduction system in Wanzhou, China. *Int. J. Disaster Risk Reduct.* **2016**, *19*, 379–389. [[CrossRef](#)]
8. Chen, T.; Zhu, L.; Niu, R.Q.; Trinder, C.J.; Peng, L.; Lei, T. Mapping landslide susceptibility at the Three Gorges Reservoir, China, using gradient boosting decision tree, random forest and information value models. *J. Mt. Sci.* **2020**, *17*, 670–685. [[CrossRef](#)]
9. Xiao, T.; Yin, K.; Yao, T.; Liu, S. Spatial prediction of landslide susceptibility using GIS-based statistical and machine learning models in Wanzhou County, Three Gorges Reservoir, China. *Acta Geochim.* **2019**, *38*, 654–669. [[CrossRef](#)]
10. Xiao, T.; Segoni, S.; Chen, L.; Yin, K.; Casagli, N. A step beyond landslide susceptibility maps: A simple method to investigate and explain the different outcomes obtained by different approaches. *Landslides* **2020**, *17*, 627–640. [[CrossRef](#)]
11. Tang, M.; Xu, Q.; Yang, H.; Li, S.; Iqbal, J.; Fu, X.; Cheng, W. Activity law and hydraulics mechanism of landslides with different sliding surface and permeability in the Three Gorges Reservoir Area, China. *Eng. Geol.* **2019**, *260*, 105212. [[CrossRef](#)]
12. Huang, X.; Guo, F.; Deng, M.; Yi, W.; Huang, H. Understanding the deformation mechanism and threshold reservoir level of the floating weight-reducing landslide in the Three Gorges Reservoir Area, China. *Landslides* **2020**, *17*, 2879–2894. [[CrossRef](#)]
13. Yang, B.; Yin, K.; Xiao, T.; Chen, L.; Du, J. Annual variation of landslide stability under the effect of water level fluctuation and rainfall in the Three Gorges Reservoir, China. *Environ. Earth Sci.* **2017**, *76*, 1–17. [[CrossRef](#)]
14. Jiang, Q.; Wei, W.; Xie, N.; Zhou, C. Stability analysis and treatment of a reservoir landslide under impounding conditions: A case study. *Environ. Earth Sci.* **2016**, *75*, 2. [[CrossRef](#)]
15. Sun, H.Y.; Pan, P.; Lü, Q.; Wei, Z.L.; Xie, W.; Zhan, W. A case study of a rainfall-induced landslide involving weak interlayer and its treatment using the siphon drainage method. *Bull. Eng. Geol. Environ.* **2019**, *78*, 4063–4074. [[CrossRef](#)]
16. Geertsema, M.; Cruden, D.M.; Schwab, J.W. A large rapid landslide in sensitive glaciomarine sediments at Mink Creek, north-western British Columbia, Canada. *Eng. Geol.* **2006**, *83*, 36–63. [[CrossRef](#)]
17. Loi, D.H.; Quang, L.H.; Sassa, K.; Takara, K.; Dang, K.; Thanh, N.K.; Van Tien, P. The 28 July 2015 rapid landslide at Ha Long City, Quang Ninh, Vietnam. *Landslides* **2017**, *14*, 1207–1215. [[CrossRef](#)]
18. Ouyang, C.; Zhou, K.; Xu, Q.; Yin, J.; Peng, D.; Wang, D.; Li, W. Dynamic analysis and numerical modeling of the 2015 catastrophic landslide of the construction waste landfill at Guangming, Shenzhen, China. *Landslides* **2017**, *14*, 705–718. [[CrossRef](#)]
19. Bardi, F.; Raspini, F.; Frodella, W.; Lombardi, L.; Nocentini, M.; Gigli, G.; Morelli, S.; Corsini, A.; Casagli, N. Monitoring the Rapid-Moving Reactivation of Earth Flows by Means of GB-InSAR: The April 2013 Capriglio Landslide (Northern Apennines, Italy). *Remote Sens* **2017**, *9*, 165. [[CrossRef](#)]
20. Liang, X.; Gui, L.; Wang, W.; Du, J.; Ma, F.; Yin, K. Characterizing the Development Pattern of a Colluvial Landslide Based on Long-Term Monitoring in the Three Gorges Reservoir. *Remote Sens.* **2021**, *13*, 224. [[CrossRef](#)]
21. Angeli, M.G.; Pasuto, A.; Silvano, S. A critical review of landslide monitoring experiences. *Eng. Geol.* **2000**, *55*, 133–147. [[CrossRef](#)]
22. Ehrlich, M.; da Costa, D.P.; Silva, R.C. Behavior of a colluvial slope located in Southeastern Brazil. *Landslides* **2018**, *15*, 1595–1613. [[CrossRef](#)]
23. Gischig, V.; Preisig, G.; Eberhardt, E. Numerical investigation of seismically induced rock mass fatigue as a mechanism contributing to the progressive failure of deep-seated landslides. *Rock Mech. Rock Eng.* **2016**, *49*, 2457–2478. [[CrossRef](#)]
24. Fan, L.; Lehmann, P.; Or, D. Effects of hydromechanical loading history and antecedent soil mechanical damage on shallow landslide triggering. *J. Geophys. Res. Earth Surf.* **2015**, *120*, 1990–2015. [[CrossRef](#)]
25. Liu, J.; Xu, Q.; Wang, S.; Subramanian, S.S.; Wang, L.; Qi, X. Formation and chemo-mechanical characteristics of weak clay interlayers between alternative mudstone and sandstone sequence of gently inclined landslides in Nanjiang, SW China. *Bull. Eng. Geol. Environ.* **2020**, *79*, 4701–4715. [[CrossRef](#)]
26. Bovenga, F.; Pasquariello, G.; Pellicani, R.; Refice, A.; Spilotro, G. Landslide monitoring for risk mitigation by using corner reflector and satellite SAR interferometry: The large landslide of Carlantino (Italy). *Catena* **2017**, *151*, 49–62. [[CrossRef](#)]
27. Meng, Q.; Li, W.; Raspini, F.; Xu, Q.; Peng, Y.; Ju, Y.; Casagli, N. Time-series analysis of the evolution of large-scale loess landslides using InSAR and UAV photogrammetry techniques: A case study in Hongheyan, Gansu Province, Northwest China. *Landslides* **2021**, *18*, 251–265. [[CrossRef](#)]
28. Zhao, C.; Zhang, Q.; He, Y.; Peng, J.; Yang, C.; Kang, Y. Small-scale loess landslide monitoring with small baseline subsets interferometric synthetic aperture radar technique—case study of Xingyuan landslide, Shaanxi, China. *J. Appl. Remote Sens.* **2016**, *10*, 026030. [[CrossRef](#)]
29. Mondini, A.C.; Santangelo, M.; Rocchetti, M.; Rossetto, E.; Manconi, A.; Monserrat, O. Sentinel-1 SAR amplitude imagery for rapid landslide detection. *Remote Sens.* **2019**, *11*, 760. [[CrossRef](#)]
30. Tarchi, D.; Casagli, N.; Fanti, R.; Leva, D.D.; Luzi, G.; Pasuto, A.; Silvano, S. Landslide monitoring by using ground-based SAR interferometry: An example of application to the Tessina landslide in Italy. *Eng. Geol.* **2003**, *68*, 15–30. [[CrossRef](#)]
31. Bardi, F.; Raspini, F.; Ciampalini, A.; Kristensen, L.; Rouyet, L.; Lauknes, T.R.; Casagli, N. Space-borne and ground-based InSAR data integration: The Åknes test site. *Remote Sens.* **2016**, *8*, 237. [[CrossRef](#)]

32. Uhlemann, S.; Smith, A.; Chambers, J.; Dixon, N.; Dijkstra, T.; Haslam, E.; Meldrum, P.; Merritt, A.; Gunn, D.; Mackay, J. Assessment of ground-based monitoring techniques applied to landslide investigations. *Geomorphology* **2016**, *253*, 438–451. [[CrossRef](#)]
33. Ferrigno, F.; Gigli, G.; Fanti, R.; Intrieri, E.; Casagli, N. GB-InSAR monitoring and observational method for landslide emergency management: The Montaguto earthflow (AV, Italy). *Nat. Hazards Earth Syst. Sci.* **2017**, *17*, 845–860. [[CrossRef](#)]
34. Casagli, N.; Frodella, W.; Morelli, S.; Tofani, V.; Ciampalini, A.; Intrieri, E.; Lu, P. Spaceborne, UAV and ground-based remote sensing techniques for landslide mapping, monitoring and early warning. *Geoenviron. Disasters* **2017**, *4*, 1–23. [[CrossRef](#)]
35. Dong, J.; Zhang, L.; Li, M.; Yu, Y.; Liao, M.; Gong, J.; Luo, H. Measuring precursory movements of the recent Xinmo landslide in Mao County, China with Sentinel-1 and ALOS-2 PALSAR-2 datasets. *Landslides* **2018**, *15*, 135–144. [[CrossRef](#)]
36. Intrieri, E.; Raspini, F.; Fumagalli, A.; Lu, P.; Del Conte, S.; Farina, P.; Casagli, N. The Maoxian landslide as seen from space: Detecting precursors of failure with Sentinel-1 data. *Landslides* **2018**, *15*, 123–133. [[CrossRef](#)]